

Metasurface Integrated Monolayer Exciton Polariton

Yueyang Chen,^{∇†} Shengnan Miao,^{∇†} Tianmeng Wang,^{∇†} Ding Zhong, Abhi Saxena, Colin Chow, James Whitehead, Dario Gerace, Xiaodong Xu, Su-Fei Shi, and Arka Majumdar*

Cite This: <https://dx.doi.org/10.1021/acs.nanolett.0c01624>

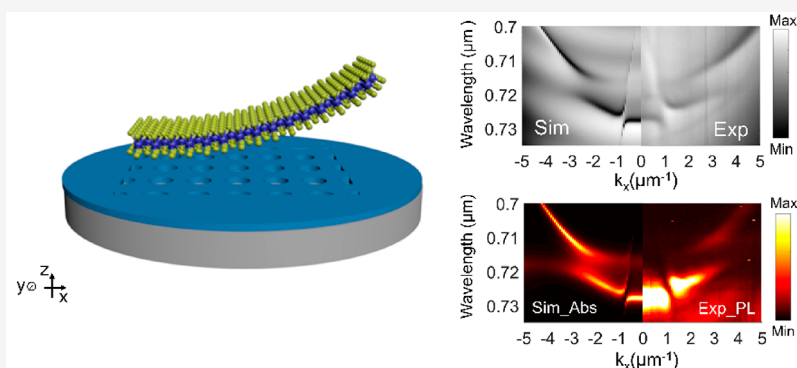
Read Online

ACCESS |

Metrics & More

Article Recommendations

Supporting Information



ABSTRACT: Monolayer transition-metal dichalcogenides (TMDs) are the first truly two-dimensional (2D) semiconductor, providing an excellent platform to investigate light–matter interaction in the 2D limit. The inherently strong excitonic response in monolayer TMDs can be further enhanced by exploiting the temporal confinement of light in nanophotonic structures. Here, we demonstrate a 2D exciton–polariton system by strongly coupling atomically thin tungsten diselenide (WSe_2) monolayer to a silicon nitride (SiN) metasurface. Via energy–momentum spectroscopy of the WSe_2 –metasurface system, we observed the characteristic anticrossing of the polariton dispersion both in the reflection and photoluminescence spectrum. A Rabi splitting of 18 meV was observed which matched well with our numerical simulation. Moreover, we showed that the Rabi splitting, the polariton dispersion, and the far-field emission pattern could be tailored with subwavelength-scale engineering of the optical meta-atoms. Our platform thus opens the door for the future development of novel, exotic exciton–polariton devices by advanced meta-optical engineering.

KEYWORDS: Dielectric metasurface, Monolayers, 2D Exciton–polariton, Light–matter interaction

INTRODUCTION

Monolayer transition-metal dichalcogenides (TMDs) have generated active research interest in recent years due to their strong light–matter interaction and unique optoelectronic properties.¹ Thanks to the quantum confinement in the atomic layer, excitons with large binding energy can form in monolayer TMD at room temperature, exhibiting strong excitonic absorption and photoluminescence.² The strong excitonic response could be further enhanced by coupling the TMD monolayer to an optical cavity.³ In the weak coupling regime, low-threshold nanolasers^{4–7} and cavity-enhanced light-emitting diodes⁸ have been demonstrated using the TMD monolayer. In the strong coupling regime, TMD exciton–polaritons (EPs) have also been observed at room temperature.^{9–11} EPs, the hybrid light–matter quasi-particles, inherit the low effective mass from their photonic component and large nonlinear interaction strength from their excitonic component, making them a promising platform to study Bose–Einstein condensate,¹² with a far-reaching impact on quantum simulation with interacting photons.¹³ TMD EP also has potential applications in low-power nonlinear optics¹⁴ and

polariton lasers.¹⁵ Furthermore, the TMD EP inherits the unique spin-valley physics from its exciton part,¹⁶ and the optical valley hall effect of the TMD EP could be explored in this hybrid light–matter system.¹⁷

So far, most TMD-based EP devices are based on distributed Bragg reflector (DBR) cavity.^{9,18,19} The fabrication process of the DBR-sandwiched TMD platform is nontrivial since the encapsulation of the upper DBR layers often degrade the optical property of the monolayer TMD.²⁰ Open cavity structures such as the fiber cavity and single DBR structure have been explored^{21,22} to solve the problem of material degradation. However, in such platforms, it is difficult to engineer the mode or dispersion of the cavity, a capability

Received: April 15, 2020

Revised: June 8, 2020

Published: June 10, 2020

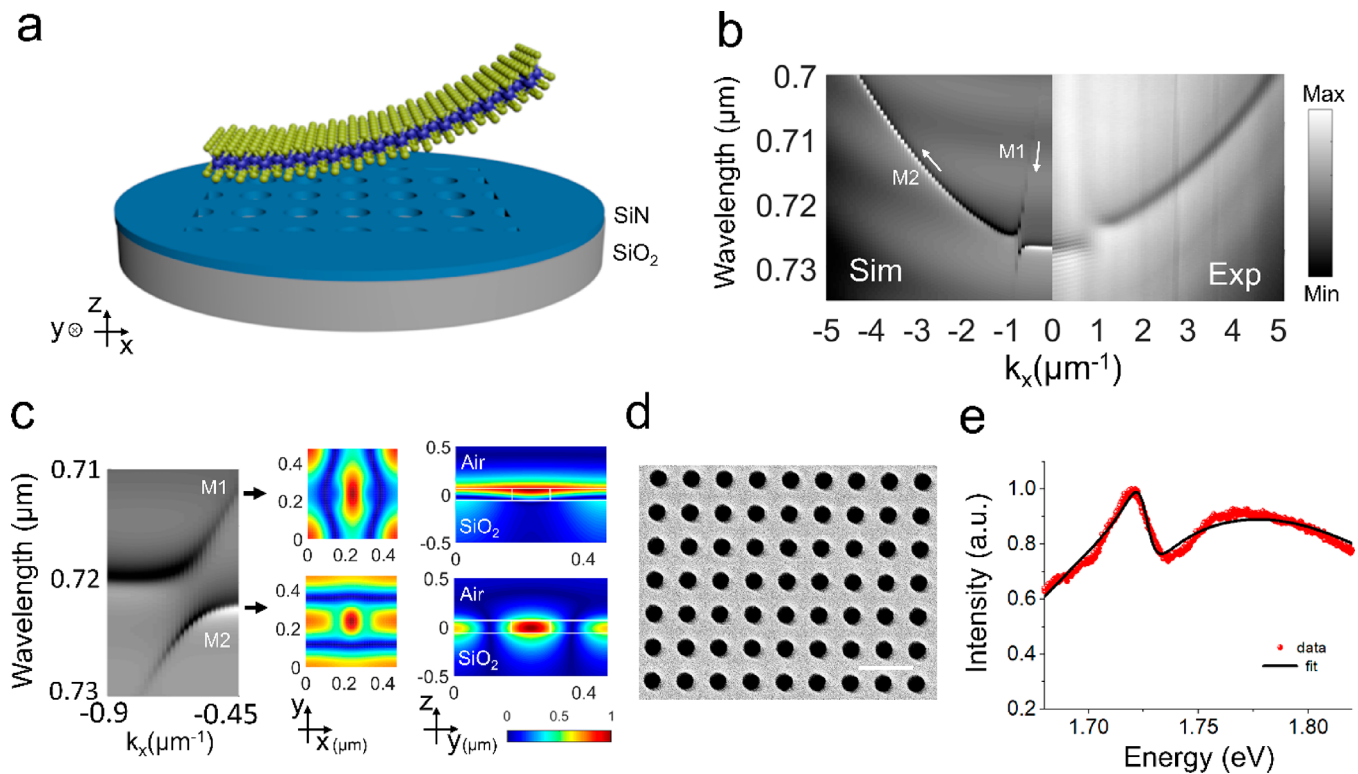


Figure 1. SiN metasurface supporting guided mode resonances: (a) The metasurface is made of SiN meta-atoms with holes arranged in a square lattice. The whole structure sits on a silicon dioxide substrate. A WSe₂ monolayer could be transferred directly on top of the metasurface for evanescent coupling. (b) Simulated vs experimentally measured angle-dependent reflection spectrum. There are two modes (M1 and M2) in the spectrum. M1 has a linear dispersion and starts at higher energy and rapidly goes to lower energy when it comes to high momentum. M2 has a parabolic shape and it starts at lower energy and goes to the higher energy. The two modes come close to each other at $k_x = 0.6 \mu\text{m}^{-1}$; an anticrossing appears due to the coupling between the two photonic modes. (c) Zoom-in of the anticrossing and the mode profiles of M1 and M2. The two modes have different symmetry in terms of the field distribution, but they are both well confined inside the metasurface. (d) The SEM of the SiN metasurface (scale bar: $1 \mu\text{m}$) (e) Example spectrum and fitting at $k_x = 2.2 \mu\text{m}^{-1}$. A Fano line shape is observed with a Q factor ~ 143 and an asymmetry factor of -1.4 .

which can have far-reaching impact in the field of exciton–polaritons. The plasmonic cavity is considered as a promising candidate,^{23–25} but it suffers from metallic loss. Another promising platform will be subwavelength patterned surfaces, also known as dielectric metasurfaces.²⁶ These metasurfaces can shape the optical wavefront using the subwavelength scatterers, also known as meta-atoms, and have recently been used to drastically miniaturize imaging and sensing devices,^{27–29} as well as to enhance light–matter interaction.^{30,31} This nanopatterned, periodic photonic lattice supports a rich cluster of optical Bloch mode and can tightly confine the electromagnetic field.^{32,33} Moreover, computational design and dispersion engineering of the meta-atoms allow unprecedented nanophotonic engineering.^{34–36} Going beyond passive metasurfaces, researchers are now exploring new materials to create active metasurfaces.^{37,38} In fact, nonlinear frequency conversion has been reported with the GaSe integrated silicon metasurface.³⁹ EP has also been demonstrated on a TMD-clad one-dimensional (1D) grating structure.⁴⁰ A signature of optical nonlinearity has recently been reported in TMD-coupled 1D bound state in a continuum resonator.⁴¹ However, extending the periodicity in two dimensions (2D) is desirable. The extra degrees of freedoms in a 2D metasurface would allow advanced dispersion engineering, providing a new opportunity to merge the EP with novel photonic designs, such as topological structures, most of which are demonstrated in two dimensions.^{42–45} Subwavelength mode engineering of

2D metasurfaces could also result in a localized optical field to further enhance the light–matter interaction.^{46,47} Finally, the intrinsic isotropic nature of the periodic 2D structure would favor the study of monolayer valley-polaritons.^{17,18} While coupling between TMD excitons and 2D periodic structure has been explored, to date, only the weak-coupling regime has been reported.^{48,49}

In this paper, we demonstrated EPs in atomically thin tungsten diselenide (WSe₂) strongly coupled to the guided mode resonances (GMR) in a silicon nitride (SiN) metasurface. The GMR simultaneously achieves strong confinement of photons inside the metasurface and efficient coupling with the radiation continuum. By performing energy–momentum spectroscopy on the WSe₂–SiN metasurface, we measured the anticrossing of the polariton dispersion both in the cavity reflection and via photoluminescence. The EP dispersion measured in the experiment is also reproduced by our numerical simulation. Moreover, we showed that the Rabi splitting, the polariton dispersion, and the far-field emission pattern could be tailored by subwavelength-scale engineering of the meta-atoms. Our platform opens the door for the future development of novel EP devices by advanced meta-optical engineering.

Guided Mode Resonances in the SiN Metasurface.

Figure 1a shows the schematic of our platform. The metasurface is made of SiN with a square lattice of holes. The whole structure sits on a silicon dioxide substrate. A WSe₂

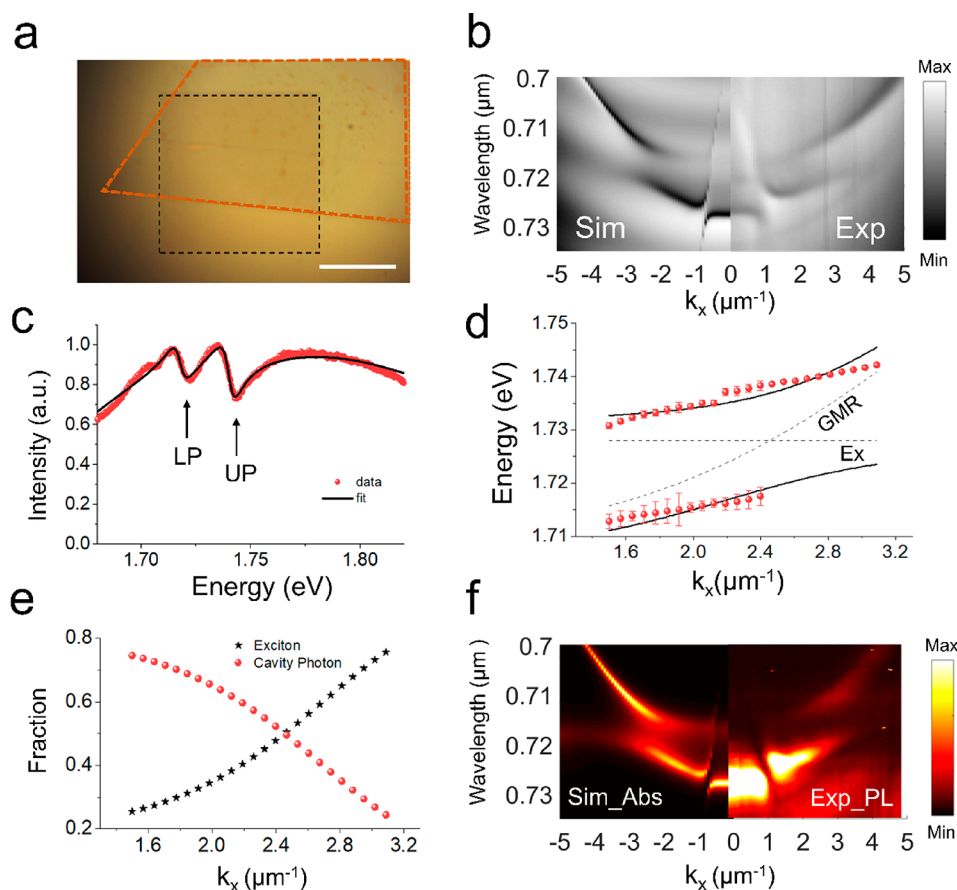


Figure 2. (a) The optical microscope image of the SiN metasurface with hBN-capped WSe₂ transferred (scale bar: 20 μm). The black lines outline the metasurface and the orange lines outline the monolayer WSe₂. The hBN is hardly observed under the microscope due to poor optical interference. (b) Simulated vs experimentally measured angle-dependent reflection spectrum. Anticrossing is observed at $k_x \sim 2.4 \mu\text{m}^{-1}$. (c) Example of a fit reflection spectrum at $k_x = 2.4 \mu\text{m}^{-1}$; the Fano-resonance of the lower polariton (LP) and upper polariton (UP) are observed. (d) Fitting for the anticrossing: a Rabi splitting value of the 18 meV is extracted. (e) Hopfield coefficients of the LP branch, which show the exciton and photon fraction in the polariton. (f) PL emission also shows the anticrossing; LPB emission is brighter than that of UPB due to the thermal equilibrium condition.

monolayer is transferred directly on top of the metasurface for evanescent coupling. Such periodic 2D photonic lattice supports many optical Bloch modes propagating inside the slab. These modes can be classified into two classes,⁵⁰ namely, in-plane guided modes and guided mode resonance (GMR). The GMRs couple with the radiation continuum and, in the meantime, confine part of their electromagnetic energy inside the slab. When a light beam shines on the metasurface, the interference between the slab mode and the GMR modes results in a Fano line shape in the reflection spectrum. These Fano resonances have been used in the past for dispersion engineering,⁵¹ spectral filtering,⁵² and enhancing the light–matter interaction.^{39,53}

We simulated the reflection spectrum of the GMR in the SiN metasurface through rigorous coupled-wave analysis (RCWA; see Methods).^{54,55} Figure 1b (left panel) shows the angle-dependent reflection spectrum along the k_x direction for p-polarized incident light. There are two GMRs, i.e., M1 has a linear dispersion and M2 has a parabolic shape. M1 starts at higher energy and goes to lower energy with higher momentum, whereas M2 starts at lower energy and goes to higher energy. Two modes come close at $k_x = 0.6 \mu\text{m}^{-1}$ and anticross due to the coupling between them. The electric field distribution of two modes at $k_x = 0$ is shown in Figure 1c. The two modes have different symmetry in terms of the field

distribution, but both are well confined inside the metasurface. We note that our metasurface acts as a cavity that stores photons and achieves field enhancement inside the slab in the vertical direction, although it does not have confinement along the in-plane directions. We confirmed the field enhancement inside the slab via RCWA simulation (Supporting Information S3).

We then fabricated the metasurface and performed energy–momentum spectroscopy at room temperature to measure the angle-dependent reflectivity spectrum. The SEM of the fabricated device is shown in Figure 1d. As shown in Figure 1b, the experimental result matches well with the simulation at the left side, with the mode-splitting observed at $k_x = 0.6 \mu\text{m}^{-1}$. The mismatch between the theory and simulation of the dispersion at high momentum can be attributed to the spherical aberration of the lenses in the optical setup. The fact that a clear photonic dispersion is measured in the momentum space clearly confirmed that we are measuring the radiative GMR mode instead of the scattering light from the in-plane guided mode, since the scattering light from the in-plane guided mode would only have a random intensity distribution in the momentum space.

We then fit the reflection spectrum $R(\omega)$ at each k_x value through a functional form:⁴⁰

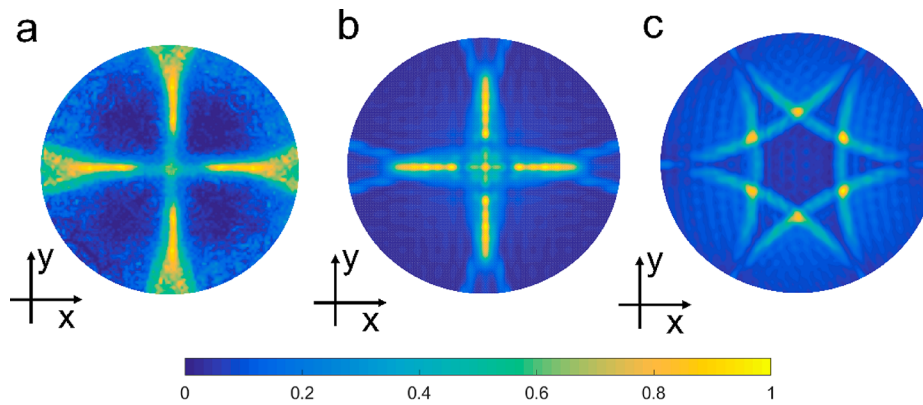


Figure 3. (a) Back focal plane (BFP) image of the far-field emission. Different from the excitonic emission of a monolayer on a unpattern substrate, the polariton emission shows a unique pattern due to the diffraction effect of the nanophotonic structures. (b) FDTD-simulated BFP image from the same metasurface structure. (c) FDTD-simulated BFP image from a hexagonal photonic lattice.

$$R(\omega) = R_{\text{Fano}} + R_{\text{FP}} + R_{\text{b}} \quad (1)$$

Here, R_{Fano} is the Fano line shape resulting from the interference of the GMR and the SiN slab mode:

$$R_{\text{Fano}} = I_0 \left(1 - \frac{(x + q)^2}{x^2 + 1} \right) \quad (2)$$

$$x = \frac{E - E_0}{\Delta\omega/2} \quad (3)$$

Here, I_0 is the amplitude coefficient of the Fano resonance, q is the asymmetry factor, $E = \hbar\omega$ is the photon energy at angular frequency of ω , $E_0 = \hbar\omega_0$ is the photon energy at the cavity resonance frequency ω_0 , and $\Delta\omega$ is the full-width at half-maximum (fwhm). Since both E_0 and $\Delta\omega$ are in units of eV, x becomes a unitless quantity. R_{FP} is a broad Fabry–Perot (FP) interference background resulting from the reflection between the SiN/SiO₂ interface and the SiO₂/Si interface. We calculate R_{FP} through the transfer matrix method⁴⁰ for the multiple thin film structure (SiN/SiO₂/Si). R_{b} represents an ambient background in the fit. Figure 1e shows an example fit for the reflection spectrum at $k_x = 2.2 \mu\text{m}^{-1}$. Through the fit, the resonance energy E_0 is extracted as 1.726 eV, the resonance Q factor as ~ 143 ($\Delta\omega = 12$ meV), and q as -1.3 .

Exciton–Polaritons in Hybrid WSe₂-Metasurface Structure. We transferred an hBN encapsulated WSe₂ monolayer on top following the usual dry transfer process.⁵⁶ The hBN encapsulation improves the surface smoothness of the WSe₂ and preserves the intrinsic narrow line width of the WSe₂.⁵⁷ We then performed the energy–momentum spectroscopy on the WSe₂–SiN metasurface structure at 22 K. As shown in Figure 2b, the GMR dispersion changed dramatically when coupled with WSe₂ at the exciton wavelength (~ 715 nm). A clear anticrossing is observed in the range from $k_x = 1.5 \mu\text{m}^{-1}$ to $k_x = 3 \mu\text{m}^{-1}$. We fit the dispersion spectrum at each k_x value with the Fano line shape function to extract the resonance wavelengths of the upper and lower polaritons. An example fit spectrum at $k_x = 2.4 \mu\text{m}^{-1}$ is shown in Figure 2c, where two Fano line shapes appear, corresponding to the upper polariton (UP) and lower polariton (LP). We note that this spectrum is dramatically different from Figure 1e where only one Fano resonance is measured as the cavity resonance. For the spectrum shown in Figure 2c (at $k_x = 2.4 \mu\text{m}^{-1}$), the resonance energy for the UP and LP is found as 1.718 and 1.74 eV, respectively, from the fitting parameters. We also observed

the anticrossing feature with another sample at 80 K (Supporting Information S2).

Once the spectrum for each k -vector is fit and the wavelengths of the UPs and LPs are extracted, we estimate the loss and the interaction strength of the coupled system. We use a dispersive coupled-oscillator model to fit the wavelength of the LPB and UPB.¹²

$$\begin{pmatrix} E_{\text{exc}} + i\gamma_{\text{exc}} & g \\ g & E_{\text{cav}} + i\gamma_{\text{cav}} \end{pmatrix} \begin{pmatrix} \alpha \\ \beta \end{pmatrix} = E_{\text{p}} \begin{pmatrix} \alpha \\ \beta \end{pmatrix} \quad (4)$$

Here, E_{exc} is the energy of the bare exciton and γ_{exc} is its decay rate. E_{cavity} is the energy of the bare cavity and γ_{cav} is the cavity decay rate; g is the coupling strength between the exciton and the cavity, and E_{p} represents the eigenvalues corresponding to the energies of the polariton modes, which could be found as

$$E_{\text{LP,UP}} = \frac{1}{2} [E_{\text{exc}} + E_{\text{cav}} + i(\gamma_{\text{cav}} + \gamma_{\text{exc}})] \pm \sqrt{g^2 + \frac{1}{4} [E_{\text{exc}} - E_{\text{cav}} + i(\gamma_{\text{exc}} - \gamma_{\text{cav}})]^2} \quad (5)$$

where α and β construct the eigenvectors and represent the weighting coefficients of the cavity photon and exciton for each polariton state, where $|\alpha|^2 + |\beta|^2 = 1$. The Hopfield coefficients which indicate the exciton and photon fraction in each LP and UP are given by the amplitude squared of the coefficients of eigenvectors ($|\alpha|^2$ and $|\beta|^2$).

Since we measured E_{cavity} before the transfer of WSe₂ and $E_{\text{LP,UP}}$ after the transfer, the independent parameters in our fit are γ_{exc} , E_{exc} , g , and γ_{cav} . During fitting, we shifted the cavity resonance (E_{cavity}) to account for the effect of the hBN and temperature dependence of the cavity resonance. Through the fitting, we extracted $E_{\text{exc}} = 1.728$ eV, $\gamma_{\text{exc}} = 6.1$ meV, $\gamma_{\text{cav}} = 8.3$ meV, and $g = 9.1$ meV. We also calculated the Rabi splitting $\hbar\Omega_{\text{Rabi}} = 2\sqrt{g^2 - \frac{1}{4}(\gamma_{\text{exc}} - \gamma_{\text{cav}})^2} = 18$ meV. This value is of the similar magnitude of the values reported using one-dimensional photonic lattice.^{40,41} To further confirm the exciton–polariton physics, we have numerically calculated the dressed modes dispersion within a quantum theoretical approach based on guided-mode expansion⁵⁸ (Supporting Information S6). We obtained an exciton–photon coupling energy $g = 11.5$ meV, i.e., a Rabi splitting ~ 23 meV when assuming f/S (oscillator strength per unit surface of the TMD

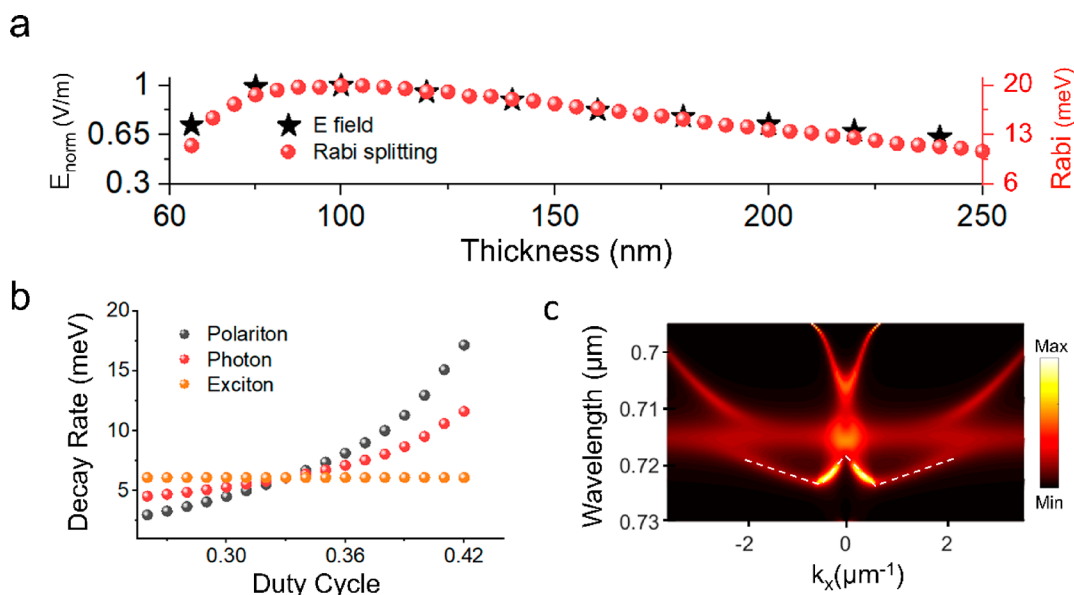


Figure 4. (a) Slab thickness-dependent Rabi splitting and normalized E field. The results indicate that a slab thickness ~ 100 nm would be the optimal thickness for enhancing the light–matter coupling strength in our platform. (b) The effect of the duty cycle of the hole in the meta-atom to the polariton decay rate. A small duty ratio would effectively suppress the polariton decay rate into the free space. (c) A unique W-shape polariton dispersion in our platform (the white dashed line).

monolayer) as the only input parameter, in remarkably good agreement with the values above.

We then compared the dissipation rate with the interaction strength to confirm that we are indeed in the strong-coupling regime. The conditions to reach strong coupling are

$$g > |\gamma_{\text{exc}} - \gamma_{\text{cav}}|/2 \text{ and } g > \sqrt{(\gamma_{\text{exc}}^2 + \gamma_{\text{cav}}^2)}/2 \quad (6)$$

Clearly, the extracted parameters ($\gamma_{\text{exc}} = 6.1$ meV, $\gamma_{\text{cav}} = 8.3$ meV, and $g = 9.1$ meV) satisfy above two criteria. We also measured photoluminescence (PL) and observed the anti-crossing in PL (Figure 2b). The PL is brighter at LPB than at UPB as expected from the thermal equilibrium condition.⁵⁹ We then calculated the angle-dependent Hopfield coefficient (α and β) from the coupled-oscillator model (eq 4). Figure 2e shows the Hopfield coefficients of the LPB. The LPB is more photon-like for $k_x < 2.4 \mu\text{m}^{-1}$ and more excitonic-like for $k_x > 2.4 \mu\text{m}^{-1}$.

Finally, we validate the experimental results with the numerical simulation. In the RCWA simulation, we added a monolayer of WSe₂ (thickness = 0.7 nm) on top of the SiN meta-atom to simulate the reflection/absorption spectrum of our WSe₂-metasurface structure (details in the Supporting Information S3). As shown in the left panels of Figure 2b and Figure 2f, our simulated reflection and absorption spectra show good agreement with the experimental reflection and PL spectra (right panels of Figure 2b and Figure 2f).

The nanopatterned subwavelength structure can also produce a directional polariton emission in the far-field. Here, we focus on the emission from the lower polariton since it is significantly brighter than the upper polariton. A 720 nm long-pass filter is placed at the collection path to block the signal from the pumping beam and the upper polariton. Figure 3a shows the back focal plane image of the spatial distribution of the collected signal. Different from the emission pattern of an in-plane exciton on an unpatterned substrate,⁶⁰ the polariton emission shows a unique pattern. The metasurface diffracts the PL signal directionally along k_x and k_y axis. We

also simulate the diffraction pattern in FDTD simulation (Figure 3b; details in the Supporting Information S5). The circumference of each figure represents the numerical aperture of the objective lens in the momentum space (NA = 0.6). We observe qualitative agreement between the experiment and simulation. We notice that the intensity of the diffraction pattern around the circumference is weaker than the experiment. This discrepancy comes from the fact that in simulation we are averaging the diffraction pattern for each wavelength inside the emission range assuming all wavelengths have identical intensity. However, in the experiment the monolayer PL emission intensity at different wavelengths is different. Interestingly, if we change the lattice into hexagonal, the simulated far-field emission pattern dramatically changes into a star shape (Figure 3c). Such ability to tailor the far-field emission pattern could be useful for polariton light-emitting devices.

Meta-optical Engineering of the Exciton–Polariton. A unique property of our metasurface-based EP is the ability to engineer the Rabi splitting, the polariton dispersion, and the far-field emission pattern by exploiting the large number of degrees of freedom offered by the nanopatterned photonic structures. Here, we systematically study how the properties of the EP can be tailored by engineering the optical meta-atoms.

We first study the effect of the metasurface thickness to the light–matter interaction strength. Different from the traditional DBR-sandwiched monolayer platform, the WSe₂ is evanescently coupled with the metasurface. Hence, the light–matter coupling strength (g) is proportional to the electric field at the surface of the meta-atoms (calculated surface field shown in Figure 4a; details in the Supporting Information S4). The surface field amplitude slightly increases as the thickness increases from 65 to 100 nm and then decreases with the further increase of the slab thickness. The results indicate a slab thickness of ~ 100 nm would be the optimal thickness for enhancing light–matter coupling in our platform. To further validate our result, we simulated the Rabi splitting of the WSe₂

coupled with the meta-atom with various thicknesses via RCWA simulation. The period of the meta-atom is adjusted while the thickness is changed to match the photonic resonance to the WSe₂ exciton wavelength (715 nm). The trend of the Rabi splitting qualitatively matches with the trend of the normalized surface electric field (Figure 4a).

We then explored the effect of the duty cycles of the hole (defined as the ratio of the hole diameter to the lattice periodicity) to the polariton decay rate. We simulated the photon decay rate as a function of the duty cycle with a fixed period and found that the decay rate increases when the hole size becomes larger (Figure 4b). Using the photon decay and experimentally extracted exciton decay rate, we calculate the polariton decay rate and find that the decay rate is suppressed with a small duty cycle. More advanced subwavelength engineering of the meta-atom could further dramatically suppress the polariton decay.⁶¹

We then analyzed the effect of the polarization and the periodicity in the EP system. Different from 1D photonic lattice, the *s* and *p* polarizations are degenerate at normal incidence ($k_x = 0$) due to the intrinsic symmetry of our metasurface. This degeneracy is lifted with gradually increasing the *k* value. Such degeneracy would allow the study of valley-polariton.¹⁸ Figure S5 in the Supporting Information shows the reflection spectrum of the *s* and *p* polarization of the metasurface before integrating it with the monolayer. A rich cluster of dispersion behavior, including linear, parabolic, and W-shape dispersion, is supported in the momentum-space of the EP system. The various slopes of dispersion favor future study of our EP platform both in the high and slow group-velocity regime, with application in ballistic propagation of polaritons⁶² and Bose–Einstein condensation.⁶¹ Figure 4c shows the simulated absorption spectrum of a hybrid structure (Supporting Information S3), where the coherent coupling of the exciton to a “W-shaped” dispersion is observed (the white dashed line), with applications in the future study of the momentum-space Josephson effect⁶² and micro-optical parametric oscillation.⁶²

In conclusion, we demonstrated EPs in atomically thin WSe₂ strongly coupled to the GMR in a SiN metasurface. The strong coupling regime is probed via energy–momentum spectroscopy on the WSe₂-metasurface sample, and a coherent light–matter interaction strength of ~18 meV is measured. Finally, we showed that the Rabi splitting, the polariton dispersion, and the far-field emission pattern could be tailored by subwavelength-scale engineering of the meta-atoms in the metasurface. Our platform opens the door for the future development of novel EP devices by advanced meta-optical engineering.

METHODS

Metasurface Fabrication. The metasurface is fabricated on 130 nm of LPCVD SiN grown on 1 μm of oxide on 500 μm of silicon substrate. We spun coat ZEP520A resist on it and patterned using a JEOL JBX6300FX with an accelerating voltage of 100 kV. The pattern was transferred to SiN using an inductive-coupled plasma etching in CHF₃/SF₆ chemistry. The ZEP520A resist is later stripped off by organic solution.

Energy–Momentum Spectroscopy. The schematic of the optical setup is shown in the Supporting Information for the reflection measurement. The white light source is sent through a beam splitter and focused onto the sample by an objective lens (NA = 0.6). The image of the reflective light at the back focal plane of the objective lens is then sent into the

spectrometer. The slit at the entrance of the spectrometer (Princeton Instruments, PIXIS CCD with an IsoPlane SCT-320 imaging spectrograph) acts as a spatial filter that only passes the signal with $k_y = 0 \mu\text{m}^{-1}$. The grating inside the spectrometer then disperses the signal ($k_x, k_y = 0 \mu\text{m}^{-1}$) to the two-dimensional CCD sensor. The dispersion of the metasurface along the ($k_x, 0$) direction is detected through the CCD, where the *x*-axis is the k_x wavevector and the *y*-axis is the wavelength. For the PL measurement, the white light source is replaced by a pumping laser (633 nm), and a 700 nm long pass filter is placed in the collection path to block the pumping laser.

Numerical Simulation. Three numerical simulation methods are used in this paper. Rigorous coupled-wave analysis (RCWA) simulation is used to simulate the angle-dependent reflection/absorption of both the metasurface sample and WSe₂-metasurface sample. We use the RCWA package (S4) developed by Stanford University.⁵³ Figures 1b, 1c, 2b, 2c, and 4c are the simulation results obtained by the RCWA simulation. The details of the RCWA simulation are discussed in the Supporting Information. A finite-difference time-domain (FDTD) solver from Lumerical Inc. is used to generate the far-field emission plot in Figures 3b and 3c. The details of the FDTD simulation are shown in the Supporting Information. Finite Element Methods via COMSOL Multiphysics software is used to solve for the Bloch eigenmodes and related results in Figure 4a and 4b. Finally, a quantum theory of exciton–photon coupling in a metasurface slab is employed in connection with a guided-mode expansion method to calculate the Rabi splitting from first principles. Details of all the simulation methods employed are given in the Supporting Information.

ASSOCIATED CONTENT

Supporting Information

The Supporting Information is available free of charge at <https://pubs.acs.org/doi/10.1021/acs.nanolett.0c01624>.

Optical setup for energy–momentum spectroscopy, anticrossing PL spectrum at 80 K, RCWA simulation for the SiN metasurface, calculation of the surface electrical field of the meta-atom, far-field simulation, and theory of exciton–photon coupling in the WSe₂–SiN metasurface (PDF)

AUTHOR INFORMATION

Corresponding Author

Arka Majumdar – *Electrical and Computer Engineering and Department of Physics, University of Washington, Seattle, Washington 98189, United States*; orcid.org/0000-0003-0917-590X; Email: arka@uw.edu

Authors

Yueyang Chen – *Electrical and Computer Engineering, University of Washington, Seattle, Washington 98189, United States*; orcid.org/0000-0002-4390-550X

Shengnan Miao – *Department of Chemical and Biological Engineering, Rensselaer Polytechnic Institute, Troy, New York 12180, United States*

Tianmeng Wang – *Department of Chemical and Biological Engineering, Rensselaer Polytechnic Institute, Troy, New York 12180, United States*

Ding Zhong – Department of Physics, University of Washington, Seattle, Washington 98189, United States

Abhi Saxena – Electrical and Computer Engineering, University of Washington, Seattle, Washington 98189, United States;

orcid.org/0000-0001-6453-929X

Colin Chow – Department of Physics, University of Washington, Seattle, Washington 98189, United States

James Whitehead – Electrical and Computer Engineering, University of Washington, Seattle, Washington 98189, United States

Dario Gerace – Department of Physics, University of Pavia, I-27100 Pavia, Italy

Xiaodong Xu – Department of Physics and Materials Science and Engineering, University of Washington, Seattle, Washington 98189, United States; orcid.org/0000-0003-0348-2095

Su-Fei Shi – Department of Chemical and Biological Engineering and Department of Electrical, Computer, and Systems Engineering, Rensselaer Polytechnic Institute, Troy, New York 12180, United States; orcid.org/0000-0001-5158-805X

Complete contact information is available at:

<https://pubs.acs.org/10.1021/acs.nanolett.0c01624>

Author Contributions

[†]These authors contributed equally to this work.

Notes

The authors declare no competing financial interest.

ACKNOWLEDGMENTS

This work is supported by the National Science Foundation under grant NSF MRSEC 1719797. S. Miao, T. Wang, and S.-F. Shi acknowledge support from AFOSR (FA9550-18-1-0312), ACS PRF (59957-DNI10), and a KIP award from RPI. Part of this work was conducted at the Washington Nanofabrication Facility/Molecular Analysis Facility, a National Nanotechnology Coordinated Infrastructure (NNCI) site at the University of Washington, which is supported in part by funds from the National Science Foundation (awards NNCI-1542101, 1337840, and 0335765), the National Institutes of Health, the Molecular Engineering & Sciences Institute, the Clean Energy Institute, the Washington Research Foundation, the M. J. Murdock Charitable Trust, Altatech, ClassOne Technology, GCE Market, Google, and SPTS.

REFERENCES

- (1) Manzeli, S.; Ovchinnikov, D.; Pasquier, D.; Yazyev, O. V.; Kis, A. 2D Transition Metal Dichalcogenides. *Nature Reviews Materials* **2017**, *2* (8), 1–15.
- (2) Wang, G.; Chernikov, A.; Glazov, M. M.; Heinz, T. F.; Marie, X.; Amand, T.; Urbaszek, B. Colloquium: Excitons in Atomically Thin Transition Metal Dichalcogenides. *Rev. Mod. Phys.* **2018**, *90* (2), 021001.
- (3) Scully, M. O.; Zubairy, M. S. *Quantum Optics* **1997**, *1*.
- (4) Wu, S.; Buckley, S.; Schaibley, J. R.; Feng, L.; Yan, J.; Mandrus, D. G.; Hatami, F.; Yao, W.; Vučković, J.; Majumdar, A.; Xu, X. Monolayer Semiconductor Nanocavity Lasers with Ultralow Thresholds. *Nature* **2015**, *520* (7545), 69–72.
- (5) Ye, Y.; Wong, Z. J.; Lu, X.; Ni, X.; Zhu, H.; Chen, X.; Wang, Y.; Zhang, X. Monolayer Excitonic Laser. *Nat. Photonics* **2015**, *9* (11), 733–737.
- (6) Li, Y.; Zhang, J.; Huang, D.; Sun, H.; Fan, F.; Feng, J.; Wang, Z.; Ning, C. Z. Room-Temperature Continuous-Wave Lasing from Monolayer Molybdenum Ditelluride Integrated with a Silicon Nanobeam Cavity. *Nat. Nanotechnol.* **2017**, *12* (10), 987–992.

(7) Ge, X.; Minkov, M.; Fan, S.; Li, X.; Zhou, W. Laterally Confined Photonic Crystal Surface Emitting Laser Incorporating Monolayer Tungsten Disulfide. *npj 2D Materials and Applications* **2019**, *3* (1), 1–5.

(8) Liu, C.-H.; Clark, G.; Fryett, T.; Wu, S.; Zheng, J.; Hatami, F.; Xu, X.; Majumdar, A. Nanocavity Integrated van Der Waals Heterostructure Light-Emitting Tunneling Diode. *Nano Lett.* **2017**, *17* (1), 200–205.

(9) Liu, X.; Galfsky, T.; Sun, Z.; Xia, F.; Lin, E.; Lee, Y.-H.; Kéna-Cohen, S.; Menon, V. M. Strong Light–Matter Coupling in Two-Dimensional Atomic Crystals. *Nat. Photonics* **2015**, *9* (1), 30–34.

(10) Dufferwiel, S.; Schwarz, S.; Withers, F.; Trichet, A. a. P.; Li, F.; Sich, M.; Del Pozo-Zamudio, O.; Clark, C.; Nalitov, A.; Solnyshkov, D. D.; Malpuech, G.; Novoselov, K. S.; Smith, J. M.; Skolnick, M. S.; Krizhanovskii, D. N.; Tartakovskii, A. I. Exciton–Polaritons in van Der Waals Heterostructures Embedded in Tunable Microcavities. *Nat. Commun.* **2015**, *6* (1), 1–7.

(11) Flatten, L. C.; He, Z.; Coles, D. M.; Trichet, A. a. P.; Powell, A. W.; Taylor, R. A.; Warner, J. H.; Smith, J. M. Room-Temperature Exciton-Polaritons with Two-Dimensional WS₂. *Sci. Rep.* **2016**, *6* (1), 1–7.

(12) Deng, H.; Haug, H.; Yamamoto, Y. Exciton-Polariton Bose–Einstein Condensation. *Rev. Mod. Phys.* **2010**, *82* (2), 1489–1537.

(13) Carusotto, I.; Ciuti, C. Quantum Fluids of Light. *Rev. Mod. Phys.* **2013**, *85* (1), 299–366.

(14) Gu, J. et al. Enhanced nonlinear interaction of polaritons via excitonic Rydberg states in monolayer WSe₂. *arXiv (Condensed Matter, Materials Science)*, December 28, 2019, 1912.12544; <https://arxiv.org/abs/1912.12544> (accessed February 18, 2020).

(15) Kim, S.; Zhang, B.; Wang, Z.; Fischer, J.; Brodbeck, S.; Kamp, M.; Schneider, C.; Höfling, S.; Deng, H. Coherent Polariton Laser. *Phys. Rev. X* **2016**, *6* (1), 011026.

(16) Sun, Z.; Gu, J.; Ghazaryan, A.; Shotan, Z.; Considine, C. R.; Dollar, M.; Chakraborty, B.; Liu, X.; Ghaemi, P.; Kéna-Cohen, S.; Menon, V. M. Optical Control of Room-Temperature Valley Polaritons. *Nat. Photonics* **2017**, *11* (8), 491–496.

(17) Lundt, N.; Dusanowski, E.; Sedov, E.; Stepanov, P.; Glazov, M. M.; Klemmt, S.; Klaas, M.; Beierlein, J.; Qin, Y.; Tongay, S.; Richard, M.; Kavokin, A. V.; Höfling, S.; Schneider, C. Optical Valley Hall Effect for Highly Valley-Coherent Exciton-Polaritons in an Atomically Thin Semiconductor. *Nat. Nanotechnol.* **2019**, *14* (8), 770–775.

(18) Chen, Y.-J.; Cain, J. D.; Stanev, T. K.; Dravid, V. P.; Stern, N. P. Valley-Polarized Exciton–Polaritons in a Monolayer Semiconductor. *Nat. Photonics* **2017**, *11* (7), 431–435.

(19) Dufferwiel, S.; Lyons, T. P.; Solnyshkov, D. D.; Trichet, A. a. P.; Withers, F.; Schwarz, S.; Malpuech, G.; Smith, J. M.; Novoselov, K. S.; Skolnick, M. S.; Krizhanovskii, D. N.; Tartakovskii, A. I. Valley-Addressable Polaritons in Atomically Thin Semiconductors. *Nat. Photonics* **2017**, *11* (8), 497–501.

(20) Sercombe, D.; Schwarz, S.; Pozo-Zamudio, O. D.; Liu, F.; Robinson, B. J.; Chekhovich, E. A.; Tartakovskii, I. I.; Kolosov, O.; Tartakovskii, A. I. Optical Investigation of the Natural Electron Doping in Thin MoS₂ Films Deposited on Dielectric Substrates. *Sci. Rep.* **2013**, *3* (1), 1–6.

(21) Sidler, M.; Back, P.; Cotlet, O.; Srivastava, A.; Fink, T.; Kroner, M.; Demler, E.; Imamoglu, A. Fermi Polaron-Polaritons in Charge-Tunable Atomically Thin Semiconductors. *Nat. Phys.* **2017**, *13* (3), 255–261.

(22) Barachati, F.; Fieramosca, A.; Hafezian, S.; Gu, J.; Chakraborty, B.; Ballarini, D.; Martinu, L.; Menon, V.; Sanvitto, D.; Kéna-Cohen, S. Interacting Polariton Fluids in a Monolayer of Tungsten Disulfide. *Nat. Nanotechnol.* **2018**, *13* (10), 906–909.

(23) Lee, B.; Liu, W.; Naylor, C. H.; Park, J.; Malek, S. C.; Berger, J. S.; Johnson, A. T. C.; Agarwal, R. Electrical Tuning of Exciton–Plasmon Polariton Coupling in Monolayer MoS₂ Integrated with Plasmonic Nanoantenna Lattice. *Nano Lett.* **2017**, *17* (7), 4541–4547.

(24) Liu, W.; Lee, B.; Naylor, C. H.; Ee, H.-S.; Park, J.; Johnson, A. T. C.; Agarwal, R. Strong Exciton–Plasmon Coupling in MoS₂

Coupled with Plasmonic Lattice. *Nano Lett.* **2016**, *16* (2), 1262–1269.

(25) Wang, S.; Li, S.; Chervy, T.; Shalabney, A.; Azzini, S.; Orgiu, E.; Hutchison, J. A.; Genet, C.; Samorì, P.; Ebbesen, T. W. Coherent Coupling of WS₂ Monolayers with Metallic Photonic Nanostructures at Room Temperature. *Nano Lett.* **2016**, *16* (7), 4368–4374.

(26) Kamali, S. M.; Arbabi, E.; Arbabi, A.; Faraon, A. A Review of Dielectric Optical Metasurfaces for Wavefront Control. *Nanophotonics* **2018**, *7* (6), 1041–1068.

(27) Zhan, A.; Colburn, S.; Dodson, C. M.; Majumdar, A. Metasurface Freeform Nanophotonics. *Sci. Rep.* **2017**, *7* (1), 1–9.

(28) Phan, T.; Sell, D.; Wang, E. W.; Doshay, S.; Edee, K.; Yang, J.; Fan, J. A. High-Efficiency, Large-Area, Topology-Optimized Metasurfaces. *Light: Sci. Appl.* **2019**, *8* (1), 1–9.

(29) Arbabi, A.; Arbabi, E.; Kamali, S. M.; Horie, Y.; Han, S.; Faraon, A. Miniature Optical Planar Camera Based on a Wide-Angle Metasurface Doublet Corrected for Monochromatic Aberrations. *Nat. Commun.* **2016**, *7* (1), 1–9.

(30) Kivshar, Y. All-Dielectric Meta-Optics and Non-Linear Nanophotonics. *Natl. Sci. Rev.* **2018**, *5* (2), 144–158.

(31) Dang, N. H. M.; Gerace, D.; Drouard, E.; Trippé-Allard, G.; Lédée, F.; Mazurczyk, R.; Deleporte, E.; Seassal, C.; Nguyen, H. S. Tailoring Dispersion of Room-Temperature Exciton-Polaritons with Perovskite-Based Subwavelength Metasurfaces. *Nano Lett.* **2020**, *20*, 2113.

(32) Semmlinger, M.; Tseng, M. L.; Yang, J.; Zhang, M.; Zhang, C.; Tsai, W.-Y.; Tsai, D. P.; Nordlander, P.; Halas, N. J. Vacuum Ultraviolet Light-Generating Metasurface. *Nano Lett.* **2018**, *18* (9), 5738–5743.

(33) Semmlinger, M.; Zhang, M.; Tseng, M. L.; Huang, T.-T.; Yang, J.; Tsai, D. P.; Nordlander, P.; Halas, N. J. Generating Third Harmonic Vacuum Ultraviolet Light with a TiO₂ Metasurface. *Nano Lett.* **2019**, *19* (12), 8972–8978.

(34) Arbabi, E.; Arbabi, A.; Kamali, S. M.; Horie, Y.; Faraon, A. Controlling the Sign of Chromatic Dispersion in Diffractive Optics with Dielectric Metasurfaces. *Optica, OPTICA* **2017**, *4* (6), 625–632.

(35) Zhan, A.; Gibson, R.; Whitehead, J.; Smith, E.; Hendrickson, J. R.; Majumdar, A. Controlling Three-Dimensional Optical Fields via Inverse Mie Scattering. *Science Advances* **2019**, *5* (10), No. eaax4769.

(36) Sell, D.; Yang, J.; Doshay, S.; Yang, R.; Fan, J. A. Large-Angle, Multifunctional Metagratings Based on Freeform Multimode Geometries. *Nano Lett.* **2017**, *17* (6), 3752–3757.

(37) Chu, C. H.; Tseng, M. L.; Chen, J.; Wu, P. C.; Chen, Y.-H.; Wang, H.-C.; Chen, T.-Y.; Hsieh, W. T.; Wu, H. J.; Sun, G.; Tsai, D. P. Active Dielectric Metasurface Based on Phase-Change Medium. *Laser & Photonics Reviews* **2016**, *10* (6), 986–994.

(38) Zubyuk, V. V.; Vabishchevich, P. P.; Shcherbakov, M. R.; Shorokhov, A. S.; Fedotova, A. N.; Liu, S.; Keeler, G.; Dolgova, T. V.; Staudé, I.; Brenner, I.; Fedyanin, A. A. Low-Power Absorption Saturation in Semiconductor Metasurfaces. *ACS Photonics* **2019**, *6* (11), 2797–2806.

(39) Yuan, Q.; Fang, L.; Fang, H.; Li, J.; Wang, T.; Jie, W.; Zhao, J.; Gan, X. Second Harmonic and Sum-Frequency Generations from a Silicon Metasurface Integrated with a Two-Dimensional Material. *ACS Photonics* **2019**, *6* (9), 2252–2259.

(40) Zhang, L.; Gogna, R.; Burg, W.; Tutuc, E.; Deng, H. Photonic-Crystal Exciton-Polaritons in Monolayer Semiconductors. *Nat. Commun.* **2018**, *9* (1), 713.

(41) Kravtsov, V.; Khestanova, E.; Benimetskiy, F. A.; Ivanova, T.; Samusev, A. K.; Sinev, I. S.; Pidgayko, D.; Mozharov, A. M.; Mukhin, I. S.; Lozhkin, M. S.; Kapitonov, Y. V.; Brichkin, A. S.; Kulakovskii, V. D.; Shelykh, I. A.; Tartakovskii, A. I.; Walker, P. M.; Skolnick, M. S.; Krizhanovskii, D. N.; Iorsh, I. V. Nonlinear Polaritons in a Monolayer Semiconductor Coupled to Optical Bound States in the Continuum. *Light: Sci. Appl.* **2020**, *9* (1), 1–8.

(42) Liu, W.; Hwang, M.; Ji, Z.; Wang, Y.; Modi, G.; Agarwal, R. Z₂ Photonic Topological Insulators in the Visible Wavelength Range for Robust Nanoscale Photonics. *Nano Lett.* **2020**, *20* (2), 1329–1335.

(43) Zhen, B.; Hsu, C. W.; Lu, L.; Stone, A. D.; Soljačić, M. Topological Nature of Optical Bound States in the Continuum. *Phys. Rev. Lett.* **2014**, *113* (25), 257401.

(44) Wu, L.-H.; Hu, X. Scheme for Achieving a Topological Photonic Crystal by Using Dielectric Material. *Phys. Rev. Lett.* **2015**, *114* (22), 223901.

(45) Jin, J.; Yin, X.; Ni, L.; Soljačić, M.; Zhen, B.; Peng, C. Topologically Enabled Ultrahigh-Q Guided Resonances Robust to out-of-Plane Scattering. *Nature* **2019**, *574* (7779), 501–504.

(46) Hu, S.; Khater, M.; Salas-Montiel, R.; Kratschmer, E.; Engelmann, S.; Green, W. M. J.; Weiss, S. M. Experimental Realization of Deep-Subwavelength Confinement in Dielectric Optical Resonators. *Science Advances* **2018**, *4* (8), No. eaat2355.

(47) Hu, S.; Weiss, S. M. Design of Photonic Crystal Cavities for Extreme Light Concentration. *ACS Photonics* **2016**, *3* (9), 1647–1653.

(48) Zhang, X.; Choi, S.; Wang, D.; Naylor, C. H.; Johnson, A. T. C.; Cubukcu, E. Unidirectional Doubly Enhanced MoS₂ Emission via Photonic Fano Resonances. *Nano Lett.* **2017**, *17* (11), 6715–6720.

(49) Huang, W.; De-Eknakul, C.; Zhang, X.; Leewong, E.; Zhao, M.-Q.; Johnson, A. T. C.; Cubukcu, E. Monolayer Excitonic Emission for Imaging Spatial Dispersion of Photonic Crystals. *ACS Photonics* **2019**, *6* (9), 2312–2319.

(50) Fan, S.; Joannopoulos, J. D. Analysis of Guided Resonances in Photonic Crystal Slabs. *Phys. Rev. B: Condens. Matter Mater. Phys.* **2002**, *65* (23), 235112.

(51) Shi, Z.; Khorasaninejad, M.; Huang, Y.-W.; Roques-Carnes, C.; Zhu, A. Y.; Chen, W. T.; Sanjeev, V.; Ding, Z.-W.; Tamagnone, M.; Chaudhary, K.; Devlin, R. C.; Qiu, C.-W.; Capasso, F. Single-Layer Metasurface with Controllable Multiwavelength Functions. *Nano Lett.* **2018**, *18* (4), 2420–2427.

(52) Wang, S. S.; Magnusson, R. Theory and Applications of Guided-Mode Resonance Filters. *Appl. Opt.* **1993**, *32* (14), 2606–2613.

(53) Piper, J. R.; Fan, S. Total Absorption in a Graphene Monolayer in the Optical Regime by Critical Coupling with a Photonic Crystal Guided Resonance. *ACS Photonics* **2014**, *1* (4), 347–353.

(54) Liu, V.; Fan, S. S4: A Free Electromagnetic Solver for Layered Periodic Structures. *Comput. Phys. Commun.* **2012**, *183* (10), 2233–2244.

(55) Zhan, A.; Colburn, S.; Trivedi, R.; Fryett, T. K.; Dodson, C. M.; Majumdar, A. Low-Contrast Dielectric Metasurface Optics. *ACS Photonics* **2016**, *3* (2), 209–214.

(56) Fryett, T. K.; Chen, Y.; Whitehead, J.; Peycke, Z. M.; Xu, X.; Majumdar, A. Encapsulated Silicon Nitride Nanobeam Cavity for Hybrid Nanophotonics. *ACS Photonics* **2018**, *5*, 2176.

(57) Cadiz, F.; Courtade, E.; Robert, C.; Wang, G.; Shen, Y.; Cai, H.; Taniguchi, T.; Watanabe, K.; Carrere, H.; Lagarde, D.; Manca, M.; Amand, T.; Renucci, P.; Tongay, S.; Marie, X.; Urbaszek, B. Excitonic Linewidth Approaching the Homogeneous Limit in MoS₂-Based van Der Waals Heterostructures. *Phys. Rev. X* **2017**, *7* (2), 021026.

(58) Gerace, D.; Andreani, L. C. Quantum Theory of Exciton-Photon Coupling in Photonic Crystal Slabs with Embedded Quantum Wells. *Phys. Rev. B: Condens. Matter Mater. Phys.* **2007**, *75* (23), 235325.

(59) Wang, J.; Su, R.; Xing, J.; Bao, D.; Diederichs, C.; Liu, S.; Liew, T. C. H.; Chen, Z.; Xiong, Q. Room Temperature Coherently Coupled Exciton–Polaritons in Two-Dimensional Organic–Inorganic Perovskite. *ACS Nano* **2018**, *12* (8), 8382–8389.

(60) Schuller, J. A.; Karaveli, S.; Schiros, T.; He, K.; Yang, S.; Kymissis, I.; Shan, J.; Zia, R. Orientation of Luminescent Excitons in Layered Nanomaterials. *Nat. Nanotechnol.* **2013**, *8* (4), 271–276.

(61) Koshelev, K. L.; Sychev, S. K.; Sadrieva, Z. F.; Bogdanov, A. A.; Iorsh, I. V. Strong Coupling between Excitons in Transition Metal Dichalcogenides and Optical Bound States in the Continuum. *Phys. Rev. B: Condens. Matter Mater. Phys.* **2018**, *98* (16), 161113.

(62) Franke, H.; Sturm, C.; Schmidt-Grund, R.; Wagner, G.; Grundmann, M. Ballistic Propagation of Exciton–Polariton Con-

densates in a ZnO-Based Microcavity. *New J. Phys.* **2012**, *14* (1), 013037.